Upper ocean hydrographic changes in response to the evolution of the East Asian monsoon in the northern South China Sea during the middle to late Miocene

Ce Yang, Haowen Dang, Xiaoli Zhou, Hongrui Zhang, Xingxing Wang, Yue Wang, Peijun Qiao, Xiaoying Jiang, Zhimin Jian

PII: S0921-8181(21)00063-1

DOI: https://doi.org/10.1016/j.gloplacha.2021.103478

Reference: GLOBAL 103478

To appear in: *Global and Planetary Change*

Received date: 2 December 2020

Revised date: 23 February 2021

Accepted date: 29 March 2021

Please cite this article as: C. Yang, H. Dang, X. Zhou, et al., Upper ocean hydrographic changes in response to the evolution of the East Asian monsoon in the northern South China Sea during the middle to late Miocene, *Global and Planetary Change* (2021), https://doi.org/10.1016/j.gloplacha.2021.103478

Upper ocean hydrographic changes in response to the evolution of the East Asian monsoon in the northern South China Sea during the middle to late Miocene

Ce Yang[a,] *, Haowen Dang[a], Xiaoli Zhou[a], Hongrui Zhang[b], Xingxing Wang[a], Yue Wang[a], Peijun Qiao[a], Xiaoying Jiang[a], Zhimin Jian[a]

[a]State Key Laboratory of Marine Geology, Tongji University, 200092 Shanghai, China

[b]Department of Earth Sciences, ETH, Zurich, Sonnegstrasse 5, 8092 Zurich, Switzerland

*corresponding author: ceyang@tongji.edu.cn

Keypoints:

1. Variations in the surface hydrography and upper ocean thermal structure were reconstructed in the South China Sea over 13.6-7.3 Ma;

2. The local $\delta^{18}O_{SW}$ of Site U1501 suggested an increase in the rainfall intensity of the East Asian summer monsoon (EASM) during 10.2-7.3 Ma;

3. Variations in the EASM rainfall are most likely linked to the initial formation of the western Pacific warm pool (WPWP) and uplift of Tibetan Plateau during 10.2-7.3 Ma.

ABSTRACT

The evolution of the East Asian monsoon (EAM) in the geologic time is of great importance to our understanding of the global climate system. However, variations in

the monsoon rainfall and the upper ocean thermal gradient are not well understood in the South China Sea (SCS) during the middle to late Miocene. Here, we present $\delta^{18}O$ and Mg/Ca-derived temperature records of the surface and subsurface waters from International Ocean Discovery Program (IODP) Site U1501, and use them to reconstruct the upper ocean thermal structure, which reflects changes in the East Asian summer monsoon (EASM) in the SCS over 13.6-7.3 Ma. The differences between the surface and thermocline records ($\Delta\delta^{18}O_{surface\text{-}thermocline}$ and $\Delta T_{surface\text{-}thermocline}$) indicate a shallower thermocline and increased thermal gradient between the surface and subsurface waters, implying that upper water mixing was weaker during 9.4-7.3 Ma, which may relate to an increased EASM rainfall. Changes in the local seawater $\delta^{18}O_{seawater}$ ($\delta^{18}O_{SW}$) of U1501 also suggest a decrease in the intensity of the EASM rainfall during 13.6-10.2 Ma and an increase during 10.2-7.3 Ma. From the perspectives of moisture supply and general circulation, the initial formation of the western Pacific warm pool (WPWP) and uplift of Tibetan Plateau essentially influenced the variations in the EASM during the middle to late Miocene.

Keywords: stable isotopes, Mg/Ca-derived water temperature, local $\delta^{18}O_{SW}$, upper ocean thermal structure, East Asian Monsoon, South China Sea, IODP Site U1501

1. Introduction

The middle to the late Miocene (13.8-5.3 Ma) represents a critical period from a unipolar warmhouse to a bipolar icehouse with prominent tectonic and climate changes in several aspects, such as the East Antarctic Ice-sheet Expansion (EAIE), the initial formation of the western Pacific warm pool (WPWP), and the uplift of the Tibetan Plateau, as well as the development of the Indian/South Asian and East Asian monsoon (An et al., 2001; Zachos et al., 2001; Jian et al., 2006). These climate or tectonic events prominently influenced the Asian monsoon, a primary component of the earth's climate system, and thus the upper ocean thermal structure and hydrological changes in the SCS during the mid-to-late Miocene. As a part of the Asian monsoon system, seasonal changes in atmospheric circulation over the SCS not only control the precipitation and river run-off, but also lead to strong seasonality in the strength and direction of ocean currents, sea surface temperature (SST), and salinity in the SCS (Wang et al., 2009). Therefore, to understand the Asian monsoon system, it is of great importance to reconstruct the upper ocean thermal structure and hydrological changes in the SCS during this time interval.

Investigating the monsoon variability and dynamics in the geological time is a crucial and challenging subject in paleoclimatology. Previous studies successfully used isotope records of surface and thermocline dwelling planktic foraminiferal species to reconstruct the upper ocean thermal structure, which reflects variations in the east Asian monsoon (EAM) during the Pleistocene (Jian et al., 2001; Tian et al., 2005; Jin and Jian, 2007; Steinke et al., 2010a). However, it is still not fully

understood how the upper ocean thermal structure in the SCS varies with changes in the EAM over million-year timescales. Indeed, the monsoon precipitation-related evidence of the EAM for the Miocene has been derived from the records of mineralogy, sedimentology, and vegetation in the SCS during ODP Leg 184 (Jia et al., 2003; Wei et al., 2006; Wan et al., 2008; Clift et al., 2014;). Nonetheless, it is controversial whether these weathering proxy records can be viewed as precipitation signals in the SCS during the late Cenozoic due to provenance shifts and productivity changes (Ren et al., 2020). The local seawater $\delta^{18}O$ ($\delta^{18}O_{SW}$) reflects sea surface salinity, and thus is a widely used proxy for monsoon rainfall during the Pleistocene (Nürnberg., 2000; Steinke et al., 2010a). Only in a few cases this proxy has been applied to the pre-Pleistocene, mainly in the northern SCS (Holbourn et al., 2010; Steinke et al., 2010b).

Here, we use surface $\delta^{18}O_{SW}$ record to reconstruct the hydrography of the surface waters in the northern SCS and reconstruct variations in the rainfall of the EAM region and the upper ocean thermal gradient of the northern SCS from 13.6 to 7.3 Ma using stable oxygen isotope and Mg/Ca-based water temperatures of the mixed layer and thermocline dwelling planktic foraminifera at International Ocean Discovery Program (IODP) Site U1501 in the SCS (Fig. 1).

2. Material and Methods

2.1 Material and age model

IODP Site U1501 (18°53.09′N, 115°45.94′E; water depth 2846 m) was drilled by

JOIDES Resolution in 2018 at a broad regional basement high in the northern SCS (Fig.1) and is well above the modern carbonate compensation depth (CCD) of the SCS (3500~4000 m) (Wang et al., 1995). A total of 102 samples were taken from Site U1501 every ~20 cm between 100.02-142.06 m core depth below seafloor (CSF-A). According to the shipboard preliminary age model, this is equivalent to a time resolution of ~20 kyr over the middle to late Miocene (Sun et al., 2018). Bulk sediment samples were dried in the oven at 60 ℃ over 24 h, weighed, and then washed through a 63 μm sieve. Foraminiferal specimens of monospecific species were picked from the coarse fraction and analyzed for carbon and oxygen stable isotopes and Mg/Ca ratio, which were performed in the State Key Laboratory of Marine Geology of Tongji University. The age model of IODP U1501 at the interval of 100-142.06 m CSF-A was established based on the linear sedimentation of 3 magnetic polarity datum and 1 $^{87}Sr/^{86}Sr$ data point (Sun et al., 2018; Jian et al., 2019) (Fig. 2).

2.2 Stable oxygen isotopes

Well-preserved (clean and intact) planktic foraminiferal shells of mixed-layer dwelling species *Globigerinoides sacculifer* (without sac-like final chamber) and the thermocline species *Neogloboquadrina acostaensis*, *Neogloboquadrina humerosa*, and *Paragloborotalia siakensis* (Pearson and Wade, 2009; Aze et al. 2011) were picked from the 250-355 μm size fraction of the washed samples with a temporal resolution of ~40 kyr for the oxygen and carbon stable isotope analysis. 7-8

specimens were cleaned in ethanol (99.7%) in an ultrasonic bath, dried in an oven at 60 ℃, and finally reacted with orthophosphoric acid in an automated carbonate device (Kiel V) at 70 ℃ to generate CO_2. The gaseous samples were transferred to a Finnigan MAT 252 mass spectrometer for measuring the stable isotopes of carbon and oxygen (Cheng et al., 2005). The isotopic results were calibrated into Pee Dee Belemnite (PDB) scale by the China National standard NBS 19 with a standard deviation of 0.07‰ for $\delta^{18}O$.

2.3 Mg/Ca paleothermometry

The measurements of Mg/Ca ratio were performed at the temporal resolutions of ~20-30 and ~40-60 kyr for the mixed layer species and thermocline species, respectively. Approximately 30-40 foraminiferal tests of *G. sacculifer*, *N. acostaensis*, *N. humerosa*, and *P. siakensis* were cleaned following the cleaning procedure of Barker et al. (2003) and Martin and Lea (2002). Foraminiferal tests were cleaned with ultra-sonication and rinses to remove clays, followed by oxidation cleaning to remove organic matter, reductive cleaning step to remove Mn-Fe-oxide coatings, and a final acid leach to remove any adsorbed contaminants. Thereafter, samples were dissolved, and then centrifuged for 10 minutes at 13000 rpm to remove any insoluble impurities.

Analytical reproducibility for *G. sacculifer* (n = 23) and *P. siakensis* (n = 5) were 2.09±0.07% and 2.06±0.07% with one standard deviation, respectively. Measured Al/Ca ratios of *G. sacculifer* and *P. siakensis* were below 0.026 mmol/mol, which were not correlated with Mg/Ca ratios ($r^2 < 0.02$), suggesting that the silicate minerals

did not affect Mg/Ca values. Mn/Ca ratios of *G. sacculifer*, *N. acostaensis*, *N. humerosa* and *P. siakensis* did not show significant correlations with Mg/Ca ratios of these four species (r^2 = 0.20, r^2 = 0.15, r^2 = 0.39, and r^2 = 0.001, respectively, Fig. S1), indicating that the Mg/Ca values were not influenced by post-depositional Mn-rich oxide coatings.

To derive seawater temperature from foraminiferal Mg/Ca records, firstly, we correct Mg/Ca values using seawater Mg/Ca ratios of the past and present following equation (Evans and Müller, 2012):

$$Mg/Ca_{test} = \frac{Mg/Ca^{t=t}_{sw}}{Mg/Ca^{t=0}_{sw}}{}^{H} \quad (1)$$

where Mg/Ca_{test} and Mg/Ca_{sw} represent Mg/Ca ratios of foraminiferal test and seawater, respectively. t = 0 is the present and t = t is some time in the past. *H* is a constant to be calibrated for a specific species. Seawater Mg/Ca ratios in the past are derived from Evans and Müller (2012). *H* for *G. sacculifer* is derived from the culture experiments in Delaney et al. (1985), and for simplicity, *H* for thermocline species are assumed to be the same as the mixed layer species.

Thereafter, we calculate seawater temperature using the corrected Mg/Ca data following the Mg/Ca-temperature calibrations for each species. Based on sediment trap samples in the northern SCS, the relationship between Mg/Ca of *G. sacculifer* and SST can be described as follows (Anand et al., 2003; Huang et al., 2008):

$$Mg/Ca_{test}=(0.38(\pm0.02)-0.02*\text{water depth(km)})\ \exp(0.090(\pm0.003)*SST\ (°C)) \quad (2)$$

Similarly, thermocline water temperature (TWT) is derived from Mg/Ca of thermocline species using the equation below (Anand et al., 2003; Huang, 2008):

$$Mg/Ca_{test} = 0.32\ (\pm 0.007)\ \exp\ (0.090\ (\pm 0.003) * TWT\ (°C)) \quad (3)$$

The resulting errors are on average 1.14 and 0.86 °C per unit change in SST and TWT, respectively.

2.4 Local seawater $\delta^{18}O$

The local $\delta^{18}O$ of seawater ($\delta^{18}O_{SW}$) is widely used to indicate relative changes in local surface water salinity (Nürnberg., 2000; Holbourn et al., 2010; Steinke et al., 2010b). The $\delta^{18}O_{SW}$ at IODP site U1501 is derived from the temperature-$\delta^{18}O$ equation of Bemis et al. (1998) for planktic foraminifera: $\delta^{18}O_{SW}$ (VSMOW‰) = (T(°C) - 16.5 + 4.8 * $\delta^{18}O_{calcite}$ VPDB‰))/4.8 - 0.27. In this equation, temperature (T) is derived from foraminiferal Mg/Ca values as described above, and $\delta^{18}O_{calcite}$ is the $\delta^{18}O$ of planktic foraminifera. The local $\delta^{18}O_{SW}$ derived from this equation is corrected for the influence of ice volume variations by subtracting 70% of the variations in the smoothed benthic foraminiferal $\delta^{18}O$ record at Ocean Drilling Program (ODP) Site 1146 (19°27.40′N, 116°16.37′E; water depth 2092 m; Holbourn et al., 2005, 2013, 2018; Shevenell et al. 2008). The errors in $\delta^{18}O_{SW}$ are estimated by propagating the errors introduced by the planktic foraminiferal $\delta^{18}O$ and Mg/Ca measurements, the Mg/Ca-temperature calibration, and the $\delta^{18}O$-temperature relationship. The resulting errors are on average 0.26‰ for $\delta^{18}O_{SW}$.

2.5 Statistical Transition Point Estimation

In order to evaluate the timing of transitions in monsoon proxy records for loess

magnetic susceptibility, local $\delta^{18}O_{SW}$, $\Delta\delta^{18}O_{S-T}$ and ΔT_{S-T}, we search turning points based on minimizing the difference (residual error) between linear model and the raw data (see details in the supplementary material).

3. Results

3.1 Stable oxygen isotope and $\delta^{18}O_{S-T}$

In this study, we present $\delta^{18}O$ records of the mixed layer species *G. sacculifer* (Fig. 3a) and thermocline dwellers *N. acostaensis*, *N. humerosa* and *P. siakensis* at U1501 during 13.7-7.3 Ma (Pearson and Wade, 2009; Aze et al. 2011) (Fig. 3b). The $\delta^{18}O$ records of the planktic mixed layer and thermocline species vary between -2.89~-1.04‰ and -1.92~-0.84‰, respectively.

The difference in $\delta^{18}O$ between the surface- and subsurface-dwelling planktic foraminifera ($\Delta\delta^{18}O_{S-T}$) has been used as a proxy for thermocline depth, with high/low values indicating a thin/thick mixed layer and shallower/deeper thermocline (Ravelo and Fairbanks, 1992; Ravelo and Shackleton, 1995; Jian et al., 2001). The $\Delta\delta^{18}O_{Surface-Thermocline}$ ($\Delta\delta^{18}O_{S-T}$) results at U1501 suggest a fluctuating thermocline during 13.6-9.4 Ma and a gradually shallowing thermocline from 9.4 to 7.3 Ma (Fig. 4). A single breakpoint was identified at 10.2 Ma of IODP U1501 $\Delta\delta^{18}O_{S-T}$ (Fig. S2d)

3.2 Upper ocean temperature and $\triangle T_{S-T}$

Based on Mg/Ca ratios of the mixed layer species *G. sacculifer* (Fig. 3c) and thermocline species *N. acostaensis*, *N. humerosa* and *P. siakensis* (Fig. 3d), surface

and subsurface seawater temperatures were reconstructed for 13.6-7.3 Ma at U1501 in the SCS. The Mg/Ca ratios of *G. sacculifer* fluctuate between 2.69 and 4.17 mmol/mol, equivalent to the Mg/Ca-SST from 24.3 ℃ to 30.8 ℃ with an average value of 28.3 ℃ (Fig. 3c). The rapid decreasing trend of SST from ~30.8 ℃ to ~27.6°C during the 13.6-12.5 Ma supports the previous study on the East Antarctic ice sheet expansion (EAIE) by global benthic $\delta^{18}O$ isotopes (Zachos et al., 2001). A previous study suggested that chemical weathering proxies are primarily controlled by temperature at million-year timescale in the EAM region (Ren et al., 2020). The decreasing SST record of U1501 during 13.6-7.3 Ma corroborates the gradual weakening trend of chemical weathering at ODP Site 1148 during mid-to-late Miocene (Wei et al., 2006). The overall decreasing trend in SST during 13.6-7.3 Ma at U1501 is in good agreement with the gradual cooling from the mid-to-late Miocene (Zachos et al., 2001).

The Mg/Ca ratios of the thermocline species vary between 1.50 and 2.65 mmol/mol, corresponding to the Mg/Ca-TWT from 17.8 ℃ to 25.6 ℃ with an average value of 23.3 ℃ (Fig. 3e). The Mg/Ca-derived TWT at U1501 displayed a relatively stable and a decreasing tendency from 13.6 to 10.3 Ma and from 10.3 to 7.3 Ma, respectively.

Previous seawater temperature reconstructions of the surface and subsurface records indicate that TWT records display a larger amplitude than the SST records on orbital time scales, implying a crucial effect of the tropical thermocline (Jian et al., 2020). The relative changes in TWT and SST in the late Pleistocene display a similar pattern, which was attributed to a greenhouse gas forcing and a potential link to the

tropical Pacific and the Southern Ocean (Gu and Philander, 1997; Luo et al., 2017; Jian et al., 2020). Therefore, it is reasonable to speculate that the variations in the thermocline temperature in the SCS on million-year time scales might be linked to the tropical Pacific and the Southern Ocean during the Miocene. Notably, the TWT signals at Site U1501 markedly decreased from 10.3 Ma to 7.3 Ma. According to the ventilated thermocline theory of the modern oceanic general circulation, we suggest that the long-term decreasing trend in TWT at U1501 is most likely linked to the middle and high latitude cooling during 10.3-7.3 Ma (Luyten et al., 1983; Huang et al., 2012; Herbert et al. 2016). The ΔT_{S-T} fluctuated around 3 °C with relatively strong vertical mixing during 13.6-9.3 Ma and weakening water mixing from 9.4 to 7.3 Ma. A single breakpoint was identified at 9.4 Ma of IODP U1501 ΔT_{S-T} (Fig. S2 e).

4.Discussion

4.1 Response of U1501 records to EAM during the mid-to-late Miocene

$\Delta\delta^{18}O_{S-T}$ and ΔT_{S-T} have been successfully used to reconstruct the upper ocean vertical structure in the SCS during the mid-to-late Pleistocene (Jian et al., 2001; Tian et al., 2005; Jin and Jian, 2007). Likewise, assuming the $\Delta\delta^{18}O_{S-T}$ and ΔT_{S-T} proxies are applicable to the Miocene, these records suggest a deepened thermocline and decreased thermal gradient between the surface and subsurface waters in the northern SCS during13.6-12 Ma, respectively (Fig. 4e, d). This implies a stronger vertical mixing during this time interval compared to the late Miocene. Different from the

long-term oscillation in the $\Delta\delta^{18}O_{S-T}$ and ΔT_{S-T} records during 13.6-9.3 Ma, the local $\delta^{18}O_{SW}$ shows a gradual decreasing tendency, most likely reflecting the decrease of monsoonal rainfall from 13.6 to 10.2 Ma (Fig. 4c). Former studies inferred that global cooling may have decreased the amount of moisture in the atmosphere and further weakening of the monsoonal rainfall (Jiang and Ding, 2008; Lu and Guo 2013). Hence, it is inferred that the decreased monsoonal rainfall at SCS may be controlled by the global cooling during 13.6-10.2 Ma.

In contract to the mid-Miocene, the $\Delta\delta^{18}O_{S-T}$ and ΔT_{S-T} records suggest that the thermocline was shallower and the thermal gradient between the surface and subsurface waters increased from 9.4 to 7.3 Ma. Statistical analysis of breakpoints in the local $\delta^{18}O_{SW}$ data indicates a breakpoint at 9.6 Ma at ODP 1146 and 10.2 Ma at IODP U1501, forming a distinct step change (Fig. S2b, c, respectively). Our local $\delta^{18}O_{SW}$ estimates imply a pronounced shift towards lower salinity of the surface water from 10.2 to 7.3 Ma, which is most likely ascribed to the strengthened monsoonal rainfall. A similar signal is observed in $\delta^{18}O_{SW}$ changes of ODP 1146 during 9.6-7.3 Ma (Fig. S2), which have been interpreted as variations in river run-off from the Pearl River (Fig. 4b) (Steinke et al., 2010b). Changes in $\delta^{18}O_{SW}$ at Sites U1501 and 1146 reveal that surface water mass in the northern SCS might have been prominently fresher around 9.5 Ma (Steinke et al., 2010b). Lighter values of *G. sacculifer* $\delta^{18}O$ of U1501 may be due to fresh water supply by EASM rainfall (precipitation and runoff), which would increase the $\Delta\delta^{18}O_{S-T}$ and lead to a weaker mixing (Fig. 4d). Furthermore, the black carbon $\Delta^{13}C$ ratios at ODP 1148, which is adjacent to Site

U1501, also suggest a slight humid tendency from 10 to 8 Ma (Jia et al., 2003).

Moreover, this strengthened EASM rainfall signal is recorded not only in marine sediment in the SCS, but also in the loess magnetic susceptibility records retrieved at Jianzha Basin (Fig. 4a), which is under the influence of EASM and record a breakpoint at 9.2 Ma (Fu et al., 2017) (Fig. S2a). It implies that these maritime and terrestrial sites have captured the same signal of EASM during this period. However, the chemical weathering record at ODP 1148 is inconsistent with our results of monsoon signal during 13.6-7.3 Ma (Clift et al., 2008), in fact, the reliability of using chemical weathering index as a proxy for precipitation intensity is still controversial due to the complexity of weathering processes (Ren et al., 2020). Accordingly, the local $\delta^{18}O_{SW}$ reconstructions for IODP U1501 might provide more reliable evidence for the EASM rainfall variations during the mid-to-late Miocene.

4.2 Comparison of EASM and SAM during 13.6-7.3 Ma

As discussed above, the results of loess magnetic susceptibility at Jianzha Bansin, local $\delta^{18}O_{SW}$ of ODP1146, local $\delta^{18}O_{SW}$ of IODP1501, $\Delta\delta^{18}O_{S\text{-}T}$ of IODP1501 and $\Delta T_{S\text{-}T}$ of IODP1501 showed breakpoints at 9.2 Ma, 9.6 Ma, 10.2 Ma, 9.4 Ma, and 9.4 Ma, respectively. Although the starting time of increased monsoon rainfall signal in these proxies are slightly different, various maritime and terrestrial records have been retrieved from the east Asia that are characterized by increased EASM rainfall from ~9.5 Ma to 7.3 Ma. (Jia et al., 2003; Steinke et al., 2010b; Fu et al., 2017). Therefore, it is suggested that the increased East Asian monsoon precipitation signal is credible

during this period.

As for South Asian monsoon (SAM) records, the monsoon wind proxy, i.e., the abundance of planktic foraminifera *Globigerina bulloides*, from the western Arabian Sea exhibits a major excursion at ~8.5 Ma, which indicates the establishment of monsoon-related upwelling (Kroon et al., 1991) (Fig. 5b). However, subsequent research on precipitation-related proxy, such as $\delta^{18}O$ changes of equid tooth records from Siwaliks, suggests a significant decrease in annual rainfall during 10-6.3 Ma (Nelson, 2005). Furthermore, hydrogen isotopic ratios of leaf wax at ODP Site 722 and pollen and leaf from Himalaya also indicate that the source regions for the plant waxes became drier and precipitation gradually decreased from 10 Ma to 7 Ma, 11 Ma to 6 Ma, respectively (Quade et al., 1995, Huang et al., 2007) (Fig. 5b).

The above-mentioned proxies suggest increased monsoon precipitation in EASM and decreased monsoon precipitation in SAM during ~10-7 Ma. To investigate the opposite variations in monsoon rainfall between the EASM and SAM during the mid-to-late Miocene, water vapor supply and circulation changes have to be considered.

From a perspective of moisture supply today, the WPWP, which is described as a key role in heat and moisture transfer in global climate, prominently influences the surface circulation and the EASM variations in the SCS (Nitta, 1987; Huang and Sun, 1998; Webster, 1994; Trenberth et al., 1998). Therefore, we hypothesize that the variations in the EASM rainfall may be under the influence of the initial formation of the WPWP during the mid-to-late Miocene. Previous studies implied that the initial

WPWP formed around 11-10 Ma (Jian et al., 2006; Li et al., 2006; Nathan et al., 2009). The decreased EASM rainfall in the SCS during 13.6-10 Ma was likely due to a lack of vapor supply before the initial formation of WPWP. In contrast, along with the initial formation of the WPWP, more vapor was transported from the WPWP to the SCS, causing an enhanced moisture supply and thus increased monsoon rainfall in the SCS from 10 to 7.3 Ma.

From the perspective of atmospheric circulation, changes in the elevation and the spatial range of the northern Tibetan Plateau influenced atmospheric circulation and moisture transport in the surrounding area prominently, and thus affected EAM intensity. (An et al., 2001; Guo et al., 2002; Kutzbach, 2004; Molnar, 2005; Liu and Dong, 2013). A recent study of the general circulation model suggests that EAM is mainly controlled by changes in paleogeography (Farnsworth et al., 2019). This is because changing paleogeography has exerted a significant effect on hydrologic evolution by disturbing atmospheric and oceanic circulations and thus energy fluxes during the geological period (Barron et al., 1990; Valdes et al., 1996). Specifically, modeling results of the full Tibetan Plateau experiment indicate that the uplift of the Tibetan Plateau influenced atmospheric circulation and caused much more precipitation over the East Asian region and less precipitation over the northern India (Chen et al., 2014).

Previously published thermochronological data from the northern Qilian, Altun, Helan, Liupan, Jishi, and northern Qinling Mountains proved that a significant uplift of the northern Tibetan Plateau occurred approximately 10-7 Ma (Jolivet et al., 2001;

Zheng et al., 2010; Lease et al., 2011; Liu et al., 2013). This simulation result and thermochronological data is in good agreement with the decreased precipitation and the shift in vegetation from wet to dry in the Indian subcontinent during the late Miocene (Quade et al., 1995; Nelson, 2005; Huang et al., 2007; Molnar et al., 2012).

5. Conclusions

We constructed the oxygen isotope and Mg/Ca-derived surface and thermocline water temperatures at IODP U1501 to evaluate the surface hydrological and upper water structure changes in the northern SCS during the mid-to-late Miocene. The overall decreasing trend in the sea surface temperature (SST) and thermocline temperature (TWT) during 13.6-7.3 Ma at U1501 is in good agreement with the gradual cooling trend from the mid-to-late Miocene suggested by other studies (Zachos et al., 2001). Variations in the local $\delta^{18}O_{SW}$ of U1501 imply an increase in the intensity of the EASM rainfall during 10.2 to 7.3 Ma. Our results of the EASM rainfall variation are also supported by other maritime and terrestrial records from ~9.5 to 7.3 Ma (Jia et al., 2003; Steinke et al., 2010b; Fu et al., 2017). For the first time, we reconstruct the upper water structure in the SCS during the mid-to-late Miocene through $\Delta\delta^{18}O_{S\text{-}T}$ and $\Delta T_{S\text{-}T}$ records, which suggest a shallower thermocline and increased thermal gradient between the surface and subsurface waters during 9.4-7.3 Ma due to fresh water supply by EASM rainfall and ensuing weaker mixing. Given the influence of the Western Pacific Warm Pool (WPWP) on surface circulation and the EASM variation in the SCS at present, the East Asian summer monsoon

(EASM) rainfall during the mid-to-late Miocene may have been influenced by the initial formation of the WPWP via its impact on the moisture supply. Likewise, the variations in the South Asian monsoon (SAM) rainfall during the late Miocene may be linked to surface cooling of the Indian Ocean and the uplift of the Tibetan Plateau. Our results and other studies suggest that the Asian monsoon rainfall is largely controlled by changes in paleogeography during the mid-to-late Miocene.

Acknowledgement

International Ocean Discovery Program (IODP) is thankfully acknowledged for providing core samples to carry out the present study. We thank the captain & crew, and scientists onboard of the IODP Expedition 368 in 2017. Dataset of this study are available on mlab.tongji.edu.cn, or upon request from ceyang@tongji.edu.cn. This work was supported by the Ministry of Natural Resources of China (grant GASI-GEOGE-04), and the Ministry of Science and Technology (grant 2018YFE0202401). We thank Xiaobo Jin for helpful discussions.

References

An, Z.S., Kutzbach, J.E., Prell, W.L., Porter, S.C., 2001. Evolution of Asian monsoons and phased uplift of the Himalaya-Tibetan plateau since Late Miocene times. Nature 411, 62-66. https://doi .org /10.1038/35075035.

Aze, T., Ezard, T.H., Purvis, A., Coxall, H.K., Stewart, D.R., Wade, B.S. and Pearson, P.N., 2011. A phylogeny of Cenozoic macroperforate planktonic foraminifera from fossil data. Biol. Rev. 86, 900-927. https://doi.org/10.1111/j.1469-185X.2011.00178.x.

Barker, S., Greaves M., Elderfield, H., 2003. A study of cleaning procedures used for foraminiferal Mg/Ca paleothermometry. Geochem. Geophys. Geosyst. 4, 8407, https://doi:10.1029/2003GC000559.

Barron, E. J., Frakes, L.A., 1990. in Phosphates of the World, Neogene to Modern phosphorites, Burnett, W. C. Riggs, S. R. Eds. Cambridge Univ. Press, International Geological Correlation Programme Project 156: Phosphorites, 3, 261-272.

Chen, G.S., Liu, Z. and Kutzbach, J.E., 2014. Reexamining the barrier effect of the Tibetan Plateau on the South Asian summer monsoon. Clim. Past. 10, 1269-1275.

https://doi.org/10.5194/cp-10-1269-2014.

Cheng, X.R., Huang, B., Jian, Z.M., Zhao, Q.H., Tian, J., Li, J.R., 2005. Foraminiferal isotopic evidence for monsoonal activity in the South China Sea: a present-LGM comparison. Mar. Micropaleontol. 54, 125-139. https://doi.org/10.1016/j.marmicro.2004.09.007.

Clift, P. D., Hodges, K. V., Heslop, D., Hannigan, R., Van Long, H., Calves, G., 2008. Correlation of Himalayan exhumation rates and Asian monsoon intensity. Nat. Geosci. 1, https://doi.org/10.1038/ngeo351.

Clift, P.D. and Plumb, R.A., 2008. The Asian monsoon: causes, history and effects (Vol. 288). Cambridge: Cambridge University Press.

Clift, P. D., Wan, S. M., Blusztajn, J. S., 2014. Reconstructing chemical weathering, physical erosion and monsoon intensity since 25 Ma in the northern South China Sea: A review of competing proxies. Earth. Sci. Rev. 130, 86-102, https://doi:10.1016/j.earscirev.2014.01.002.

Deser, C., Alexander, A., Timlin, M.S., 1996. Upper-ocean thermal variations in the North Pacific during1970-1991. J. Clim. 9, 1840-1855. https://doi.org/10.1175/1520-0442(1996)009<1840:uotvit>2.0.co;2

Elderfield, H., Ferretti, P., Greaves, M., Crowhurst, S., McCave, I.N., Hodell, D., Piotrowski, A.M., 2012. Evolution of ocean temperature and ice volume through the mid-Pleistocene climate transition. Science, 337, 704-709. https://doi.org/10.1126/science.1221294.

Evans, D., Müller, W., 2012. Deep time foraminifera Mg Ca paleothermometry: Nonlinear correction for secular change in seawater Mg/Ca. Paleoceanography 27, PA4205. https://doi.org 10.1029/2012PA002315.

Farnsworth, A., Lunt, D. J., Robinson, S. A., Valdes, P. J., Pancost, R.D., 2019. Past east Asian monsoon evolution controlled by paleogeography, not CO_2. Sci. Adv. 5. https://doi.org/10.1126/sciadv.aax1697.

Ford, H.L., Sosdian, S.M., Rosenthal, Y. and Raymo, M.E., 2016. Gradual and abrupt changes during the Mid-Pleistocene Transition. Quat. Sci. Rev. 148, 222-233. https://doi.org/10.1016/j.quascirev.2016.07.005.

Fu, C.F., Qiang, X.K., Xu, X.W., Xu, J.J., Zuo, J., An, Z.S., 2017. Late Miocene magnetostratigraphy of Jianzha basin in the northeastern margin of the Tibetan Plateau and changes in the east Asian summer monsoon. Geol. J. 53, 282-292. https://doi.org/10.1002/gj.3047.

Gu, D.F., Philander, S.G.H., 1997. Interdecadal climate fluctuations that depend on exchanges between the tropics and extratropics. Science 275, 805-807. https://doi.org/10.1126/science.275.5301.805.

Guo, Z.T., Ruddiman, W.F., Hao, Q.Z., Wu, H.B., Qiao, Y.S., Zhu, R.X., Peng, S.Z., Wei, J.J., Yuan, B.Y., Liu T.S., 2002. Onset of Asian desertification by 22 Myr ago inferred from loess deposits in China. Nature 416, 159-163. https://doi.org/10.1038/416159a.

Hall, R.,1998. The plate tectonics of Cenozoic SE Asia and the distribution of land and sea. J. Asian. Earth. Sci. 20, 99-131.

Herbert, T.D., Lawrence, K.T., Tzanova, A., Peterson, L.C., Caballero-Gill, R. and Kelly, C.S., 2016. Late Miocene global cooling and the rise of modern ecosystems. Nat. Geosci. 9, 843-847. https://doi.org/10.1038/NGEO2813.

Huang K. F., You C. F., Lin H., et al., 2008. In situ calibration of Mg/Ca ratio in planktonic 63 foraminiferal shell using time series sediment trap: A case study of intense dissolution artifact in the South China Sea. Geochem. Geophys. Geosyst. 9, 1-20. https://doi.org/10.1029/2007GC001660.

Huang, R.X., 2010. Ocean circulation: wind-driven and thermohaline processes. Cambridge University

Press.

Huang, Y.S., Clemens, S.C., Liu, W., Wang, Y., Prell, W.L., 2007. Large-scale hydrological change drove the late Miocene C4 plant expansion in the Himalayan foreland and Arabian Peninsula. Geology 35, 531-534. https://doi.org/10.1130/G23666A.1.

Huang, R.H., Sun, F.Y., 1992. Impacts of the tropical western Pacific on the East Asian summer monsoon. J. Meteorol. Soc. Jpn. Ser. II, 70, 243-256. https://doi.org/10.2151/jmsj1965.70.1B_ 243.

Holbourn, A., Kuhnt, W., Schulz, M. and Erlenkeuser, H., 2005. Impacts of orbital forcing and atmospheric carbon dioxide on Miocene ice-sheet expansion. Nature 438, 483-487. https://doi.org/10.1038/nature04123.

Holbourn, A.E., Kuhnt, W., Regenberg, M., Schulz, M., Mix, A. Andersen, N., 2010. Does Antarctic glaciation force migration of the tropical rain belt? Geology 38, 783-786. https://doi.org/ 10.1130/G31043.1.

Holbourn, A.E., Kuhnt, W., Clemens, S., Prell, W. and Andersen, N., 2013. Middle to late Miocene stepwise climate cooling: Evidence from a high-resolution deep water isotope curve spanning 8 million years. Paleoceanography 28, 688-699. https://doi.org/10.1002/2013PA002538.

Holbourn, A.E., Kuhnt, W., Clemens, S.C., Kochhann, K.G., Johnicke, J., Lübbers, J. and Andersen, N., 2018. Late Miocene climate cooling and intensification of southeast Asian winter monsoon. Nat. Commun. 9, 1-13. https://doi.org/10.1038/s41467-018-03950-1.

Jia, G., Peng, P.A., Zhao, Q.H., Jian, Z.M., 2003. Changes in terrestrial ecosystem since 30 Ma in east Asia: Stable isotope evidence from black carbon in the South China Sea. Geology 31, 1093-1096. https://doi.org/10.1130/G19992.1.

Jian, Z.M., Huang, B.Q., Kuhnt, W., Lin, H.-L., 2001. Late Quaternary upwelling intensity and east Asian monsoon forcing in the South China Sea. Quat. Res. 55, 363-370. https://doi.org/10.1006/qres.2001.2231.

Jian Z.M., Yu Y.Q., Li B.H, Wang J.L., Zhang X., Zhou Z.Y., 2006. Phased evolution of the south–north hydrographic gradient in the South China Sea since the middle Miocene. Palaeogeogr. Palaeoclimatol. Palaeoecol. 230, 251-263. https://doi.org/10.1016/j.palaeo.2005.07.018.

Jian, Z. M., Jin, H.Y., Kaminski, M.A., Ferreira, F., Li, B. and Yu, P.S., 2019. Discovery of the marine Eocene in the northern South China Sea. Natl. Sci. Rev. 6, 881-885. doi.org/10.1093/nsr/nwz084.

Jian, Z.M., Wang, Y., Ding, T.W., Lea, D.W., Liu, Z.Y., Jin, H.Y., Yin, Y.Q., 2020. Half-precessional cycle of thermocline temperature in the western equatorial Pacific and its bihemispheric dynamics. Proc. Natl. Acad. Sci. 117,7044-7051, https://doi.org/10.1073/pnas.1915510117.

Jiang H., Ding Z..2008. A 20 Ma pollen record of East-Asian summer monsoon evolution from Guyuan, Ningxia, China. Palaeogeogr. Palaeoclimatol. Palaeoecol. 265, 30-38. https://doi.org/10.1016/j.palaeo.2008.04.016.

Jin, H.Y., Jian Z.M., 2007. Paleoclimatic Instability During the Mid-Pleistocene Transition: Implications from Foraminiferal Stable Isotope at ODP Site1144, Northern South China Sea. Adv. Earth Sci. 22: 914-921. https://doi:10.11867/j.issn.1001-8166.2007.09.0914.

Jolivet, M., Brunel, M., Seward, D., Xu, Z., Wu, C., 2001. Mesozoic and Cenozoic tectonics of the northern edge of the Tibetan Plateau: fission-track constraints. Tectonophysics 343, 111-134. https://doi.org/10.1016/S0040-1951(01)00196-2.

Kitoh, A., 2004. Effects of Mountain Uplift on East Asian Summer Climate Investigated by a Coupled Atmosphere-Ocean GCM. J. Clim. 17,783-802. https://doi.org/10.1175/1520-0442(2004)017<0783:EOMUOE>2.0.CO;2

Kroon, D., Steens, T.N.F., Troelstra, S.R., 1991. Onset of Monsoonal Related Upwelling in the Western Arabian Sea as Revealed by Planktonic Foraminifers. Proc. Ocean Drill. Program Sci. Results 117. 257-263. https://doi.org/10.2973/odp.proc.sr.117.126.1991.

Kutzbach, J.E., Liu, X.D., Liu, Z.Y., Chen, G.S., 2008. Simulation of the evolutionary response of global summer monsoons to orbital forcing over the past 280,000 years. Clim. Dynam. 30, 567-579. https://doi.org/10.1007/s00382-007-0308-z.

Lease, R. O., Burbank, D. W., Clark, M. K., Farley, K. A., Zheng, D.W., Zhang H.P., 2011. Middle Miocene reorganization of deformation along the northeastern Tibetan Plateau. Geology 39, 359-362.
https://doi.org/10.1130/G31356.1.

Li, Q.Y., Li, B.H., Zhong, G.F., McGowran, B., Zhou, Z.Y., Wang, J.L., Wang, P.X., 2006. Late Miocene development of the western Pacific warm pool: Planktonic foraminifer and oxygen isotopic evidence. Palaeogeogr. Palaeoclimatol. Palaeoecol. 237, 465-482. https://doi.org/10.1016/j.palaeo.2005.12.019.

Liu, X. D., Dong, B. W., 2013. Influence of the Tibetan Plateau uplift on the Asian monsoon-arid environment evolution. Chin. Sci. Bull., 58, 4277-4291. https://doi.org/10.1007/s11434-013-5987-8

Liu, J. H., Zhang, P. Z., Lease, R. O., Zheng, D. W., Wan, J. L., Wang, W. T., Zhang, H. P., 2013. Eocene onset and late Miocene acceleration of Cenozoic intracontinental extension in the North Qinling range-Weihe graben: Insights from apatite fission track thermochronology, Tectonophysics,584, 281-296. https://doi.org/10.1016/j.tecto.2012.01.025.

Lu H. Y., Guo, Z.T. ,2014. Evolution of the monsoon and dry climate in East Asia during late Cenozoic: A review. Sci. China Earth Sci. 57,70-79. https://doi.org/10.1007/s11430-013-4790-3.

Luo, Y., Lu, J., Lu, F., Garuba, O., 2017. The role of ocean dynamical thermostat in delaying the El Nino like response over the Equatorial Pacific to climate warming. J. Clim. 30, 2811-2817. https://doi.org/10.1175/JCLI-D-16-0454.1.

Luyten, J.R., Pedlosky, J. and Stommel, H., 1983. The ventilated thermocline. J. Phys. Oceanogr. 13, 292-309. https://doi.org/10.1175/1520-0485(1983)013<0292:TVT>2.0.CO;2.

Martin, P. A. and Lea, D.W., 2002. A simple evaluation of cleaning procedures on fossil benthic foraminiferal Mg/Ca. Geochem. Geophys. Geosyst. 3, 8401. https://doi.org/10.1029/2001GC000280.

Mohtadi, M., Prange, M., Oppo, D.W., De Pol-Holz, R., Merkel, U., Zhang, X., Steinke, S., Luckge, A., 2014. North Atlantic forcing of tropical Indian Ocean climate. Nature 509, 76-80.

Molnar P., 2005. The growth of the Tibetan Plateau and Mio-Pliocene evolution of East Asian climate. Palaeontol. Electronica. 8, https://doi.org/10.1016/j.palaeo.2009.11.002.

Molnar P, Rajagopalan B., 2012. Late Miocene upward and outward growth of eastern Tibet and decreasing monsoon rainfall over the northwestern Indian subcontinent since ~10 Ma. Geophys. Res. Lett. 39, L09702. doi:10.1029/2012GL051305.

Nathan S. A., Leckie R. M., 2009. Early history of the Western Pacific Warm Pool during the middle to late Miocene (~13.2-5.8 Ma): Role of sea-level change and implications for equatorial circulation. Palaeogeogr. Palaeoclimatol. Palaeoecol. 274, 140-159. https://doi.org/10.1016/j.palaeo.2009.01.007.

Nitta, T., 1987. Convective activities in the tropical western Pacific and their impact on the Northern Hemisphere summer circulation. J. Meteorol. Soc. Jpn. Ser. II, 65, 373-390. https://doi.org/10.2151/jmsj1965.65.3_373.

Nelson, S.V., 2005. Paleoseasonality inferred from equid teeth and intra-tooth isotopic variability.

Palaeogeogr. Palaeoclimatol. Palaeoecol. 222, 122-144. https://doi.org/10.1016/j.palaeo.2005.03.012

Nürnberg, D., 2000. Taking the temperature of past ocean surfaces. Science 289, 1698-1699. https://doi.org/10.1126/science.289.5485.1698

Pearson, P.N., Wade, B.S., 2009. Taxonomy and stable isotope paleoecology of well-preserved planktonic foraminifera from the uppermost Oligocene of Trinidad. J. Foraminiferal. Res. 39, 191-217. https://doi.org/10.2113/gsjfr.39.3.191.

Quade, J., Cater, J.M., Ojha, T.P., Adam, J. and Mark Harrison, T., 1995. Late Miocene environmental change in Nepal and the northern Indian subcontinent: Stable isotopic evidence from paleosols. Geol. Soc. Am. Bull.107(12),1381-1397. https://doi.org/10.1130/0016-7606(1995)107<1381: LMECIN>2.3.CO;2.

Ravelo, A. C., Fairbanks R. G., 1992. Oxygen isotopic composition of multiple species of planktonic foraminifera: Recorders of the modern photic zone temperature gradient. Paleoceanography 7, 815-831, doi:10.1029/92PA02092.

Ravelo, A. C., Shackleton, N. J., 1995. Evidence for surface-water circulation changes at Site 851 in the eastern tropical Pacific Ocean, Proc. Ocean Drill. Program Sci. Results, 138, 503-514. http://www-odp.tamu.edu/publications/138_SR/VOLUME/CHAPTERS/sr138_22.pdf.

Ren, X., Nie, J., Saylor, J. E., Wang, X., Liu, F., Horton, B.K., 2020.Temperature control on silicate weathering intensity and evolution of the Neogene East Asian summer monsoon. Geophys. Res. Lett. 47, e2020GL088808. https://doi.org/10.1029/2020GL088808.

Shevenell, A.E., Kennett, J.P., Lea, D.W., 2008. Middle Miocene ice sheet dynamics, deep-sea temperatures, and carbon cycling: A Southern Ocean perspective. Geochem. Geophys. Geosyst. 9. https://doi.org/10.1029/2007GC001736.

Steinke, S., Mohtadi, M., Groeneveld, J., Lin, L. C., Löwemark, L., Chen, M.T., Rendle-Bühring, R., 2010a. Reconstructing the southern South China Sea upper water column structure since the Last Glacial Maximum: Implications for the East Asian winter monsoon development. Paleocenography 25, PA2219. doi:10.1029/2009PA001850, 2010.

Steinke S., Groeneveld J., Johnstone H., Rendle-Bühring, R., 2010b. East Asian summer monsoon weakening after 7.5 Ma: Evidence from combined planktonic foraminifera Mg/Ca and $\delta^{18}O$ (ODP Site 1146; northern South China Sea). Palaeogeogr. Palaeoclimatol. Palaeoecol. 289, 33-43. https://doi.org/10.1016/j.palaeo.2010.02.007.

Stöckli, R., Vermote, E., Saleous, N., Simmon, R. & Herring, D. The Blue Marble Next Generation-A True Color Earth Dataset Including Seasonal Dynamics from MODIS (NASA Earth Observatory, Goddard Space Flight Center, Greenbelt, MD, USA, 2005).

Sun Z., Jian Z.M., Stock J.M. and the Expedition 367/368 Scientists. Proc IODP 2018; 367/368 (Site U1501): 1-62. https://doi.org/10.14379/iodp.proc.367368.2018.

Tian, J., Wang, P.X., Chen, R.H. and Cheng, X.R., 2005. Quaternary upper ocean thermal gradient variations in the South China Sea: Implications for east Asian monsoon climate. Paleoceanography 20(4). PA4007, doi:10.1029/2004PA001115

Trenberth, K.E., Branstator, G.W., Karoly, D., Kumar, A., Lau, N.C., Ropelewski, C., 1998. Progress during TOGA in understanding and modeling global teleconnections associated with tropical sea surface temperature. J. Geophys. Res. 103,14291-14324. https://doi.org/10.1029/97JC01444.

Valdes, P.J., Sellwood, B.W., Price, G.D., 1996. Evaluating concepts of Cretaceous equability. Palaeoclimates. Data Model. 2, 139-158.

Wan S. M., Li A.C., Xu, K.H., Yin, X.M., 2008. Characteristics of Clay Minerals in the Northern South

China Sea and Its Implications for Evolution of East Asian Monsoon since Miocene. J. China Univ. Geosci. 19, 23-37. https://doi.org/10.1016/S1002-0705(08)60021-7.

Wang, P.X., Wang, L.J., Bian, Y.H., Jian Z.M., 1995. Late Quaternary paleoceanography of the South China Sea: surface circulation and carbonate cycles. Mar. Geol. 127, 145-165. https://doi.org/10.1016/0025-3227(95)00008-M.

Wang, P.X., Li, Q.Y., 2009. The South China Sea. Developments in Paleoenvironmental Research, 13, https://doi.org/10.1007/978-1-4020-9745-4.

Wang, L., Wu, S.G., Li, Q.P., Wang, D.W., Fu, S.Y., 2014. Architecture and development of a multi-stage Baiyun submarine slide complex in the Pearl River Canyon, northern South China Sea. Geo-Mar. Lett. 34, 327-343. https://doi.org/10.1007/s00367-014-0372-4.

Webster, P.J., 1994. The role of hydrological processes in ocean-atmosphere interactions. Reviews of Geophysics 32(4), 427-476. https://doi.org/10.1029/94RG01873.

Webster, P.J., Magaa, V. O., Palmer, T.N., Shukla, J., Tomas, R.A., Yanai, M.U., Yasunari, T., 1998. Monsoons: Processes, predictability, and the prospects for prediction. J. Geophys. Res.: Oceans, 103, 14451-14510. https://doi.org/ 10.1029/97JC02719.

Wei, G. J., Li X.H., Liu Y., Shao, L., Liang, X.R., 2006. Geochemical record of chemical weathering and monsoon climate change since the early Miocene in the South China Sea. Paleoceanography 21, PA4214. https://doi.org/10.1029/2006PA001300

Zachos J., Pagani M., Sloan L., Thomas E., Billups K., 2001. Trends, rhythms, and aberrations in global climate 65 Ma to present. Science 292, 686-693. https://doi.org/10.1126/science.1059412.

Zheng, D., Clark, M.K., Zhang, P., Zheng, W., Farley, K. A., 2010. Erosion, fault initiation and topographic growth of the north Qilian Shan (northern Tibetan Plateau). Geosphere 6, 937-941. https://doi.org/10.1130/GES00523.1.

Zhuang, G.S., Pagani, M., Zhang, Y.G., 2017. Monsoonal upwelling in the western Arabian Sea since the middle Miocene. Geology 45, 655-658. https://doi.org/10.1130/G39013.1.

Figure captions

Fig. 1. The locations of IODP U1501 (white star), ODP1146 (orange solid circle), ODP 1148 (blue solid circle), ODP 722 (purple solid circle), and Jianzha Basin (yellow solid circle). (a) Satellite image and bathymetry from Stöckli et al. (2015); (b) Paleogeographic reconstruction at 10 Ma (Simplified by Hall, 1998).

Fig. 2. Age model of U1501. Biostratigraphic, magnetostratigraphic (Sun et al., 2018), and strontium isotope stratigraphic (Jian et al., 2019) correlations at Site U1501.

Fig. 3. Oxygen isotope and Mg/Ca-derived seawater temperature records at U1501

Fig.4 Combined continental and marine proxy records of the East Asian monsoon. (a) Magnetic susceptibility of Jianzha Basin (Fu et al., 2017); (b) $\delta^{18}O_{SW}$ of ODP 1146(Steinke et al., 2010b); (c) Local δ^{18}Osw of IODP U1501; (d) $\Delta\delta^{18}O_{S\text{-}T}$ of IODP U1501; (e) $\Delta T_{S\text{-}T}$ of IODP U1501

Fig.5 Combined continental and marine proxy records of the Asian monsoon. (a)$\delta^{18}O_{SW}$ of IODP U1501; (b) hydrogen isotope ratios of leaf wax C_{31} *n*-alkane extracted from ODP Site 722 (Huang et al., 2007);

Fig. S1. Mn/Ca versus Mg/Ca ratios

Fig. S2. Change point analysis of monsoon proxy records

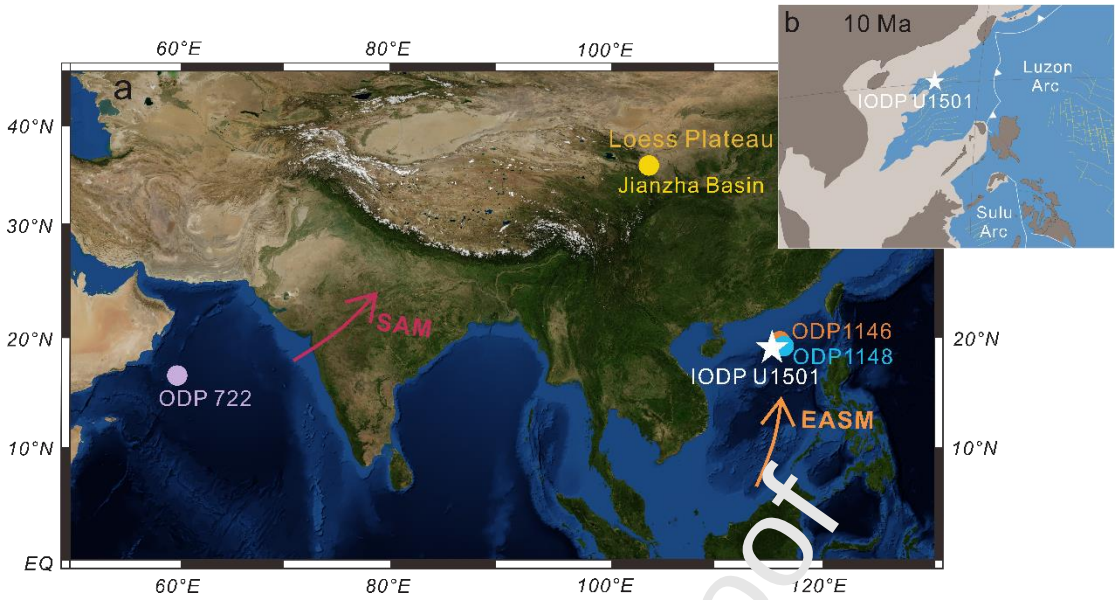

Fig. 1.

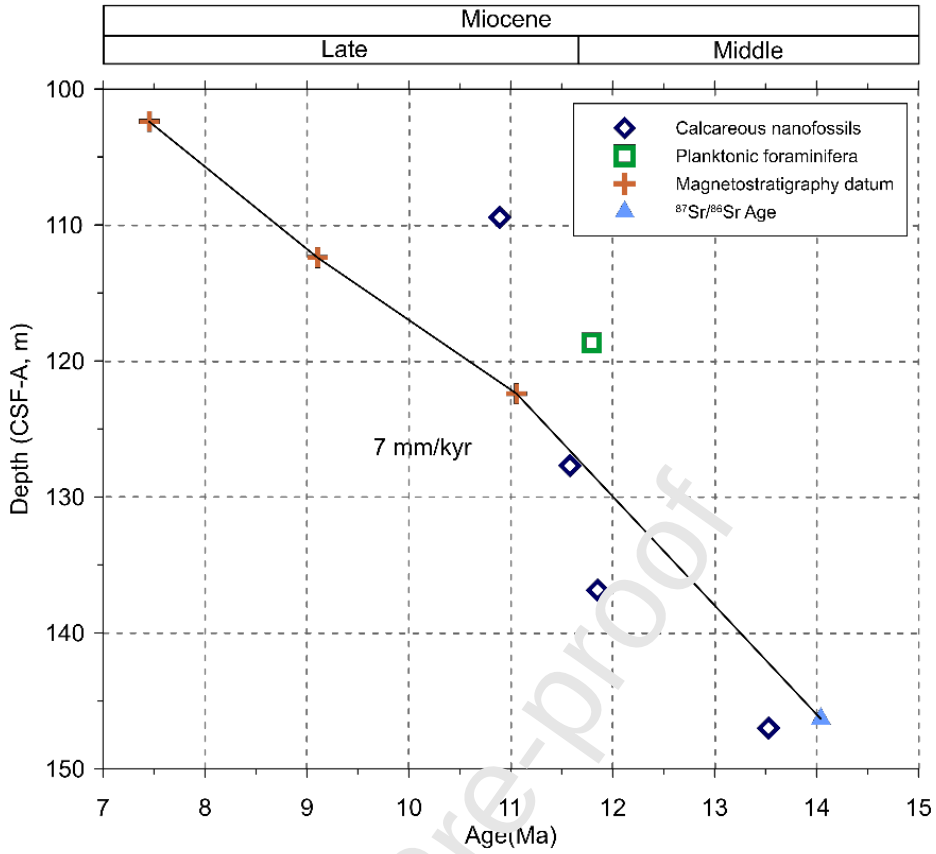

Fig. 2.

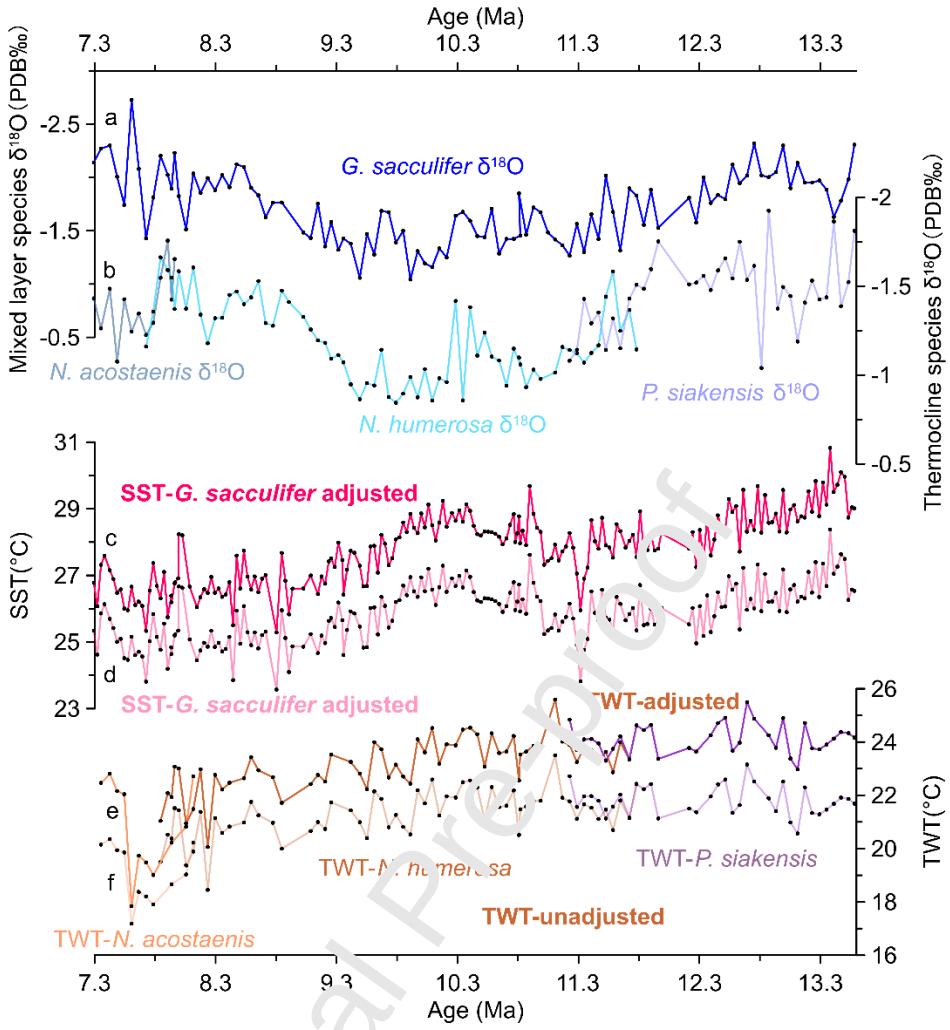

Fig. 3.

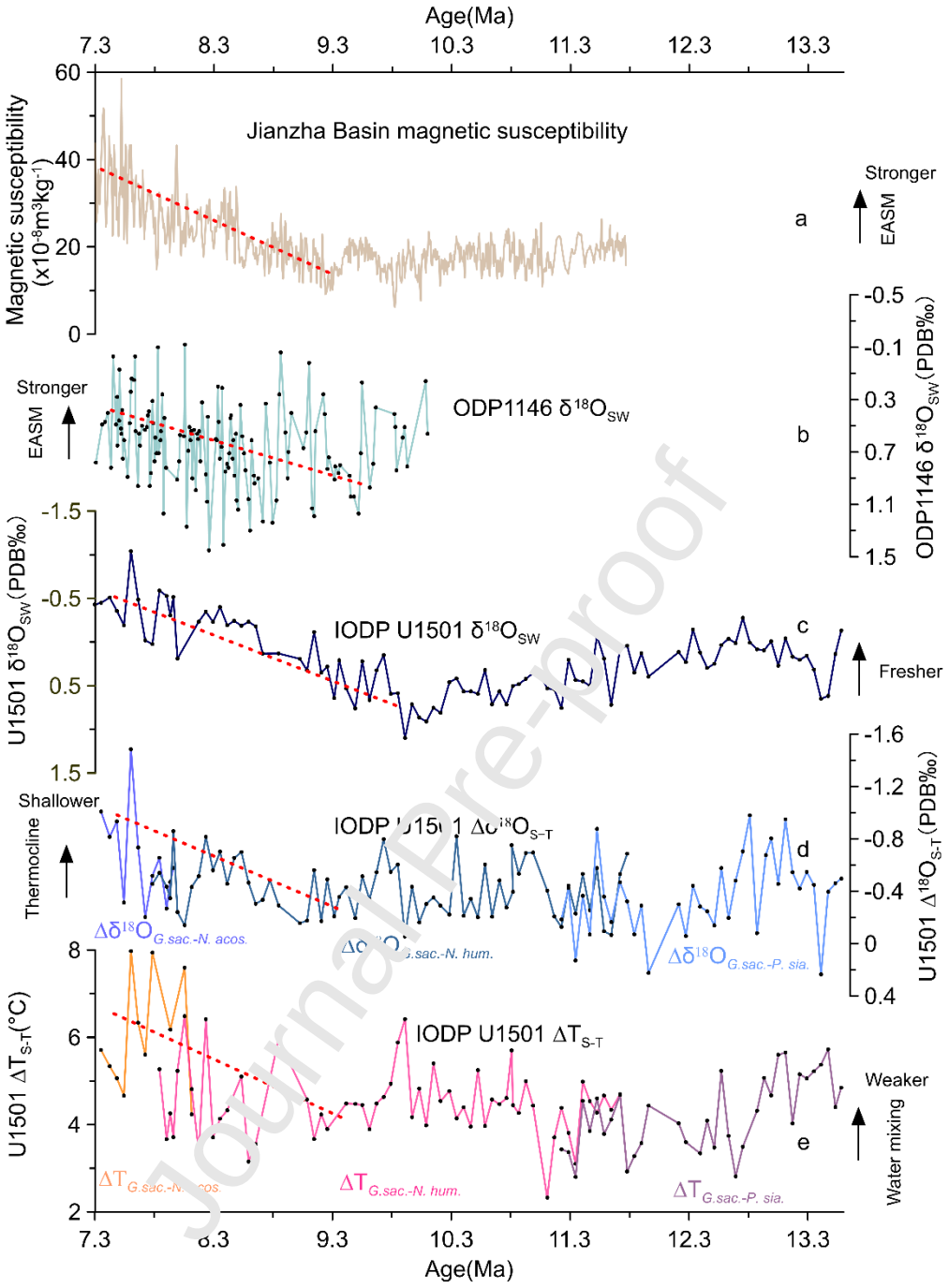

Fig. 4.

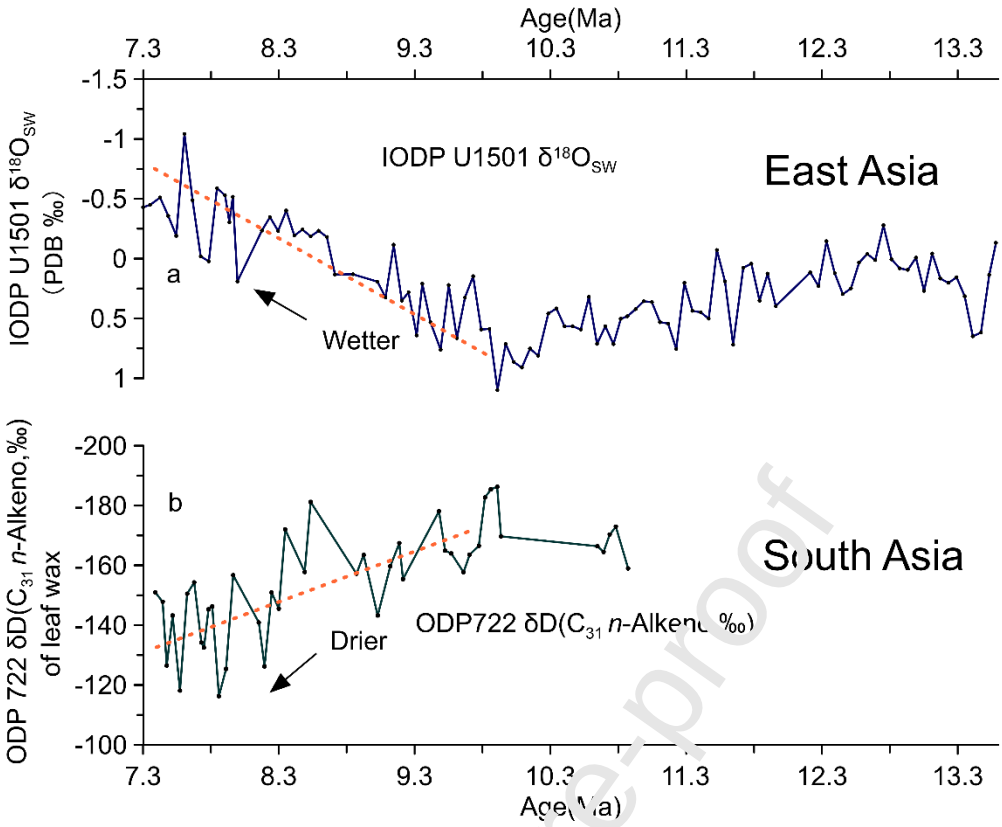

Fig. 5.

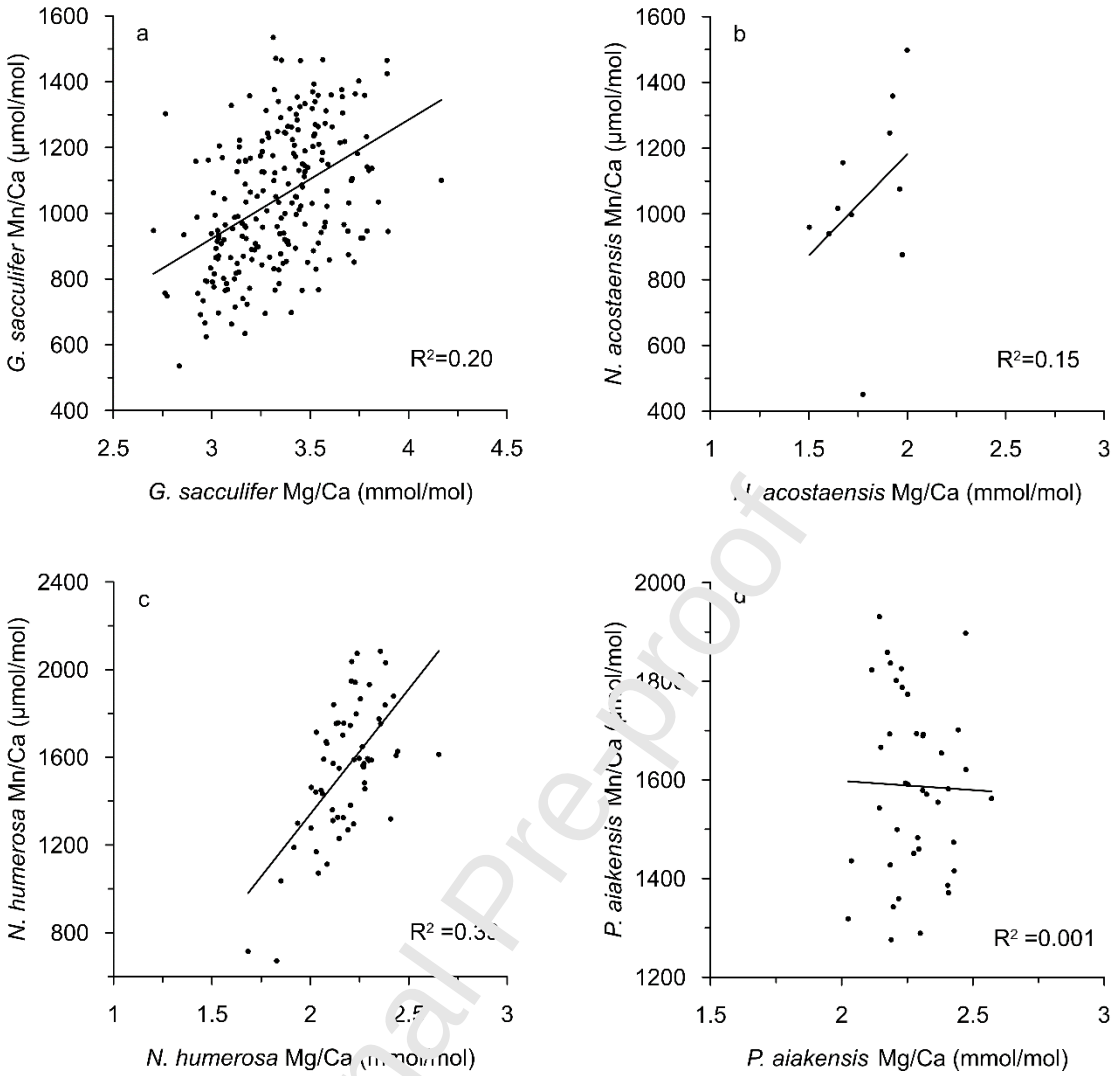

Fig. S1.

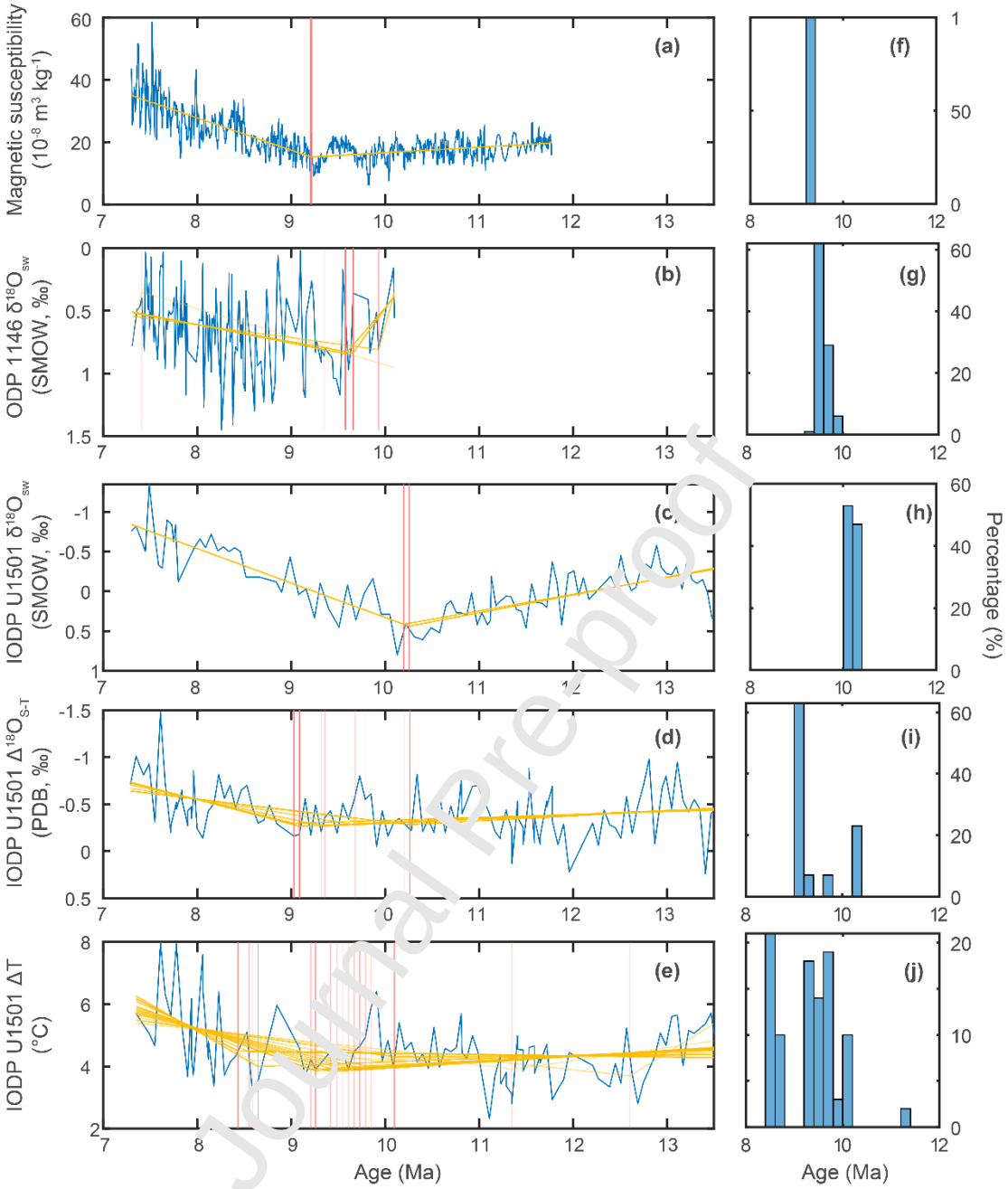

Fig. S2.

The method of searching turning point employed in this study is based on minimizing the difference (residual error) between linear model and the raw data. For a dataset with potential turning points (could be more than one), the residual error could be calculated by the following equation:

$$Residual\ error = \sum_{j=1}^{M+1}\{\sum_{i=N_{j-1}}^{N_j}\left(\frac{abs(y^{j}_{(x=x_i)} - y_{(x=x_i)})}{N_j - N_{j-1}}\right)\}$$

where M represents the number of turning points in the time series (in this study M=1), N

represents the number of data. Abs(x) is the absolute value of x. y_j is the linear fitting results of the data between N_{j-1} and N_j. The linear fitting process was performed by optimistic function 'optimset' with type of 'lsqlin' and the minimization of residual error was achieved by optimistic function 'fmincon' provided in Matlab. For each optimistic process, a guessed initial point should be given arbitrarily. However, for scatted paleoclimatology datasets, the turning points could be sensitive to the initial turning point because the minimum of residual error was trapped in a local minimum. To avoid the initial value bias, the initial values were set as randomly distributed between 12-8 Ma and the turning points were calculated by a Monte Carlo process for 100 times (Figure S2).